Aerodynamic Investigation of Shrouded Rotors with Dual Exit Channels

Abdallah Dayhoum [1,*], Alejandro Ramirez-Serrano [2], and Robert Martinuzzi [3]

[1] Mechanical and Manufacturing Engineering, University of Calgary, Canada
[2] Director UVS Robotarium Robotics Lab, Canada
[3] Pratt & Whitney Canada Research Fellow, Canada
Email: abdallah.sayed@ucalgary.ca (A.D.); aramirez@ucalgary.ca (A.R-S.); rmartinu@ucalgary.ca (R.M.)
*Corresponding author

***Abstract*—The growing need for rotary-wing aerial vehicles with high-speed forward movement and dependable hover performance is critical in various applications. Shrouded rotors enhance aerodynamic performance, create more overall thrust with the same power consumption as open rotors, and have a more uniform induced velocity flow field. This paper presents a parametric computational investigation centered on the hypothesis, that dividing the shroud exit channel into convergent inner and divergent outer channels would enhance flow uniformity, reducing power losses, and preventing airflow separation from the main shroud's inner walls. The validity of this hypothesized concept is demonstrated through extensive Computational Fluid Dynamic (CFD) simulations. The paper includes a case analysis utilizing experimental data from a highly-maneuverable drone, named Navig8, equipped with a 9-inch shrouded propeller where various shrouded configurations are examined using Computational Fluid Dynamics. Results typically show an increase in total thrust with the incorporation of an inner shroud for a given power.**

***Keywords*—shrouded rotors, rotary wings, VTOL aerodynamics**

I. Introduction

Unmanned Aerial Vehicles (UAVs) represent a topic of significant importance in scientific and aerospace engineering research, playing a crucial role in various real-world applications across both military and civilian domains [1, 2]. Vertical Take-Off and Landing (VTOL) aircraft, including quad-rotors and helicopters, pose a spectrum of challenges such as noise reduction and optimizing payload capacity given a specific power constraint [3, 4]. Conventional methods for controlling rotors in small VTOLs encounter issues with complex mechanical assemblies [5, 6]. As a solution, the use of multi-rotors with a fixed pitch setting has gained popularity in modern applications. This approach, eliminating the need for intricate swash plates, provides benefits including easier handling, cost-effectiveness, and simplicity [7, 8]. Encasing rotors within a shroud enhances open rotor efficiency, resulting in increased thrust, reduced noise, and minimized rotor tip losses, as demonstrated in studies [9–13]. Shrouded propellers, often referred to as ducted, exhibit significantly improved aerodynamic performance compared to those without a shroud. Despite the theoretical advantages, optimizing shroud and rotor combinations for minimal drag, maximum thrust, and other desired outcomes is crucial due to existing aerodynamic complexities [14].

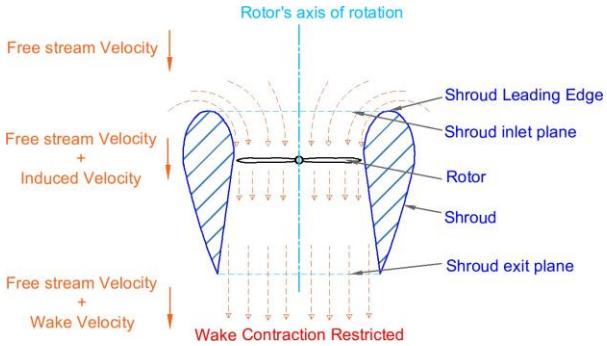

Fig. 1. Schematic cross-section diagram of a shrouded-rotor aerodynamic principle.

The air drawn in from the sides of the shroud by the rotor creates a low-pressure area, resulting in suction that enhances the shroud inlet's thrust, shown in Fig. 1. Simultaneously, the airflow in the shrouded rotor's exit channel often termed a diffuser, encounters a negative pressure gradient as it returns to ambient atmospheric pressure [15]. Furthermore, shrouding the rotor presents another benefit: it may contribute to reducing the rotor's noise [16, 17]. Overall, the effectiveness of the diffuser to prevent the natural contraction of flow (in case of an open rotor) after passing through the rotor is another aspect that gives shrouding the rotor its performance advantage [18]. The existence of a shroud can limit the increase in velocity of the far wake which reduces the induced power requirements of the rotor (assuming the flow can remain attached to the diffuser's walls) [19, 20].

When comparing an open rotor and a shrouded rotor with identical rotor disc areas and (ideal) power consumption, the shrouded rotor generally yields a greater overall thrust relative to the open rotor [14, 21]. This superiority comes from the increased mass flow through the shrouded rotor, along with a reduction in

Manuscript received January 16, 2024; revised February 20, 2024; accepted March 11, 2024; published August 7, 2024.

wake velocity. In the case of shrouded rotors, the augmented mass flow primarily results in increased induced velocity, resulting in elevated induced power at the expense of the profile power. This, in theory, should lead to a higher total thrust-to-total power ratio [22, 23]. As a result, the shroud plays a pivotal role in enhancing the inflow uniformity around enclosed rotors compared to open rotors, resulting in reduced non-uniform inflow power losses. Consequently, a comprehensive aerodynamic investigation of shrouded rotors is imperative to quantitatively identify methods for increasing thrust and mitigating power losses attributed to inflow non-uniformity. Such advancements hold substantial potential for enhancing the overall performance of VTOL aircraft [24, 25].

Exploring the aerodynamics of shrouded rotor VTOLs exposes areas for additional research and striking potential applications. Current research focuses mostly on aerodynamic benefits, however there is a significant gap in understanding complicated flow interactions within the shroud. Filling this gap is critical for improving design parameters and increasing aerodynamic efficiency. Furthermore, while thrust augmentation and noise reduction are central topics, focusing on specific applications such as urban air mobility, where aerodynamics plays an important role in maneuverability, and surveillance, which benefit from reduced acoustic signatures, will drive technological and practical advancements. Closing these aerodynamic gaps and focusing on application-driven research will help to improve the shrouded rotor VTOL environment, promoting innovations with far-reaching consequences for aerial transit and surveillance.

To this end, it is hypothesized that the inclusion of an inner channel provides a mechanism for enhancing the thrust of shrouded propellers while reducing the total power consumed. This would be accomplished by accelerating the inner part of the exit flow, aiming for a balance between the static pressure increase (shroud thrust) and maintaining the relatively high induced velocity (which reduces the profile power) along with reducing the nonuniform power losses. The incorporation of an inner shroud (with a convergent shape) also provides an opportunity to enhance the operation of shrouded rotors by directing part of the energetic flow field to the main shroud's inner walls. This aspect, in theory, provides the opportunity to prevent potential flow separation induced by an adverse pressure gradient. Building upon this hypothesis, this paper provides a set of preliminary results aimed at characterizing and comprehensively evaluating shrouded rotor configurations with Dual Exit Shrouds (DES).

II. Navig8 Shrouded Rotor

Due to the complexity associated with analysis enhancing and better understanding dual exit shrouded rotors, a case study is currently being used via a novel tilt-rotor aircraft termed the Navig8 (Fig. 2). The Navig8 family of Unmanned Aerial Vehicles (UAVs) consists of scalable, highly maneuverable VTOL aircraft capable of flying in open spaces as well as inside confined spaces. Their main application is in places that are inaccessible to helicopters, such as the interior of a collapsed structure, mine shafts, or beneath forest canopy. The ability to maneuver in small spaces and the capacity to hover and land while in a non-zero pitch, and attitude are the core capabilities shared by all Navig8 vehicles [26]. The Navig8 UAV, shown in Fig. 2, comprises twin tilting shrouded rotors flanking a central fuselage [27, 28]. The used rotor of the Navig8 is a three-blade 9-in twisted propeller (Fig. 3(a)) inside a shroud (Fig. 3(b)) as detailed in Fig. 3(c).

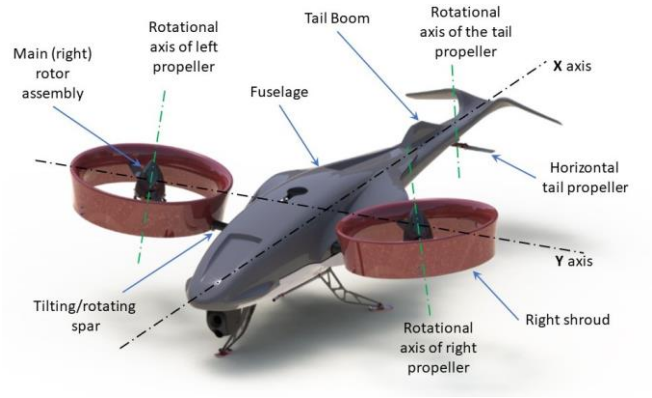

Fig. 2. Navig8 UAV prototype.

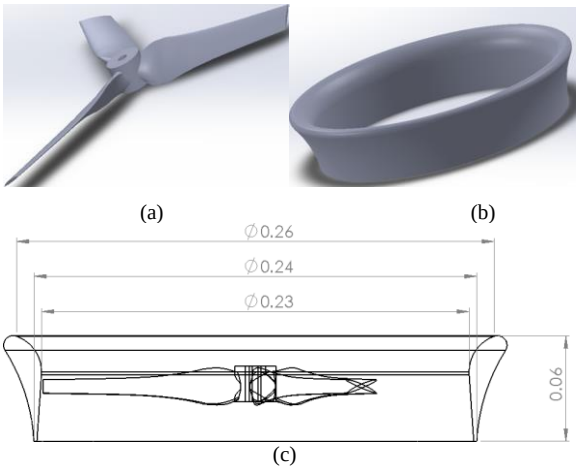

Fig. 3. Navig8's shrouded rotors: (a) 9-inch twisted rotor; (b) Navig8's shroud; (c) Detailed drawing of Navig8's shrouded rotor.

III. Inner Channel Configuration

The basic shrouded rotor described in Section II is enhanced with the addition of an inner shroud as illustrated in Fig. 4. The hypothesized inner shroud geometry introduces three primary parameters which are varied to characterize their effect on thrust and power: i) its inlet diameter (D_1), ii) outlet diameter (D_2), and iii) the shroud's length (L). Additionally, the parametric study incorporates the position offset of the inner shroud, denoted by (Z), defined as the distance between the rotor and the inner shroud inlet. The inlet diameter is selected as a function of the rotor diameter (D_R) (defined as inlet ratio, $D = D_1/D_R$), while the outer diameter is

determined as a function of the inner shroud inlet diameter (defined as contraction ratio, $C = D_2/D_1$). Both the inner shroud length and its distance from the rotor are determined as functions of the diffuser length (L_D), which is defined as the distance between the rotor and the end of the main shroud. The profile of the inner shroud wall is linear with thickness, approaching zero, as depicted in the cross-section in Fig. 4.

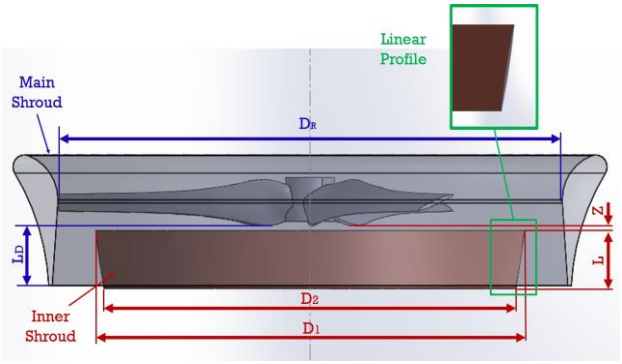

Fig. 4. Detailed drawing of Navig8's shroud with the inner channel.

Table I provides an overview of the selected values for the four parameters for the used inner shroud inside Navig8 main shrouded rotor having D_R = 0.1143 m and L_D = 0.025 m. Two distinct values for the inner shroud length were chosen: the first value ($L_1 = L_D$) ensures that the inner shroud consistently extends beyond the exit of the main shroud, while the second value ($L_2 = 0.7L_D$) ends before the main shroud exit. The chosen values for the inlet diameter of the inner shroud are positioned proximate to the high-velocity profiles of the blades, particularly near the rotor tip. The outlet diameter determines the contraction ratio of the channel, selected as a function of the inlet diameter.

TABLE I. THE USED VALUES OF THE FOUR PARAMETERS

L/L_D	$D = D_1/D_R$	$C = D_2/D_1$	Z/L_D
1	0.95	0.96	0.05
0.7	0.9	0.93	0.15
	0.85	0.9	0.25

Each configuration is designated by a code representing its specific shape (e.g., L1D95C96Z1 corresponds to the dual exit shrouded rotor with the first length of the inner shroud of $L = L_D$, an inlet diameter of $0.95D_R$, an outlet diameter of $0.96D_1$, and placed at the first position $Z_1 = 0.05L_D$, closest to the rotor). CFD simulations were conducted at a consistent rotational velocity of 10,000 rpm, reflecting the rotational velocity at which the Navig8 UAV initiates hovering. Utilizing the parameter values outlined in Table I, a total of 54 simulations were performed, exploring various configurations of the dual exit shrouded rotor. The simulations commenced with the first length, involving variations in both the inlet and outlet diameters of the inner shroud, resulting in a 3×3 matrix. For each point in this matrix, representing a distinct inner shroud shape, three different positions were employed, yielding a total of 27 unique configurations for the first length. This procedure was then replicated for the second length value resulting in a total of 54 configurations.

IV. COMPUTATIONAL MODEL

To simulate the flow structure and predict the aerodynamic performance of Navig8's dual-shrouded rotor, the CFD software ANSYS FLUENT is employed. The simulations are conducted in a steady-state, 3D, and are executed at a fixed rotational speed of 10,000 rpm for various configurations. Rotor rotation is simulated using the steady state Mixing Plane approach in this research. The entire flow field consists of two sub-domains: a stationary domain encompassing the entire computational domain and a rotating domain created to encompass the rotor, as illustrated in Fig. 5. The computational domain takes the form of a cylinder with lengths of 2.5 m (approximately equal to $11D_R$) and a diameter of 3 m (approximately equal to $13D_R$) and the shrouded rotor model is set after the stationary domain entry by 1m. The inlet boundary is set as a velocity inlet with zero velocity, and the outlet far-field boundary is configured as a pressure outlet. Walls in the stationary zone are set as symmetry boundaries, while all surfaces of the shrouded rotor configuration are defined as no-slip walls.

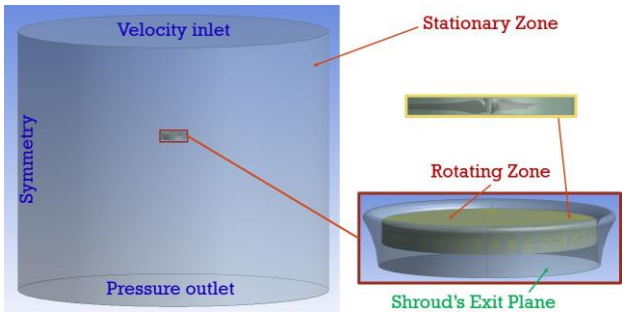

Fig. 5. Stationary and rotating domains used in the simulation.

The Realizable $k-\epsilon$ turbulence model, incorporating a standard wall function, was employed in the simulations. The pressure velocity coupling equation is solved using the Coupled scheme, and the governing equation is spatially discretized using a second-order scheme. The turbulence model is both spatially and temporally discretized using a first-order Upwind scheme. The air is assumed to have a constant density of 1.057 kg/m^3, consistent with the experimental conditions. To assess the feasibility and accuracy of the numerical method, available experimental data for the Navig8's 9-inch shrouded rotor was utilized, and the results were compared with the CFD results for an identical configuration.

V. RESULTS AND DISCUSSION

The assessment of the proposed configurations' performance is based on the total thrust, comprising rotor thrust, shroud thrust, and the added inner shroud drag, relative to the total power, encompassing profile power and induced power. Thrust values are directly obtained from Ansys, and the rotor torque is utilized to calculate

the total power. The performance of various dual exit shroud configurations is then compared with the Single Exit Shroud (SES) configuration based on the total thrust-to-power ratio. To ensure the reliability of the computational model, experimental results for the utilized Navig8 shrouded rotor are incorporated and compared with the computational results. Fig. 6 illustrates the relative agreement between the measured and calculated numerical thrust of Navig8's shrouded rotor. The figure indicates a comparatively small error, affirming the accuracy of the CFD simulation, which was subsequently applied to the dual exit shroud case.

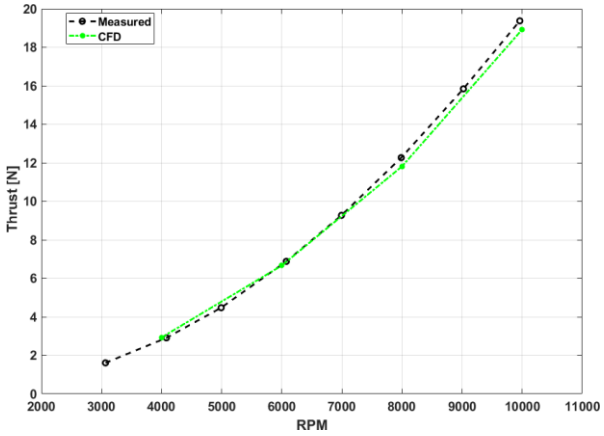

Fig. 6. Measured versus numerical total thrust.

The resulting total thrust-to-power ratio for all configurations is depicted in a bar chart, as illustrated in Fig. 7. The black bar represents the thrust-to-power ratio of the single exit shroud, while the horizontal red line serves as a reference value for comparison with other dual exit shroud configurations. The figure indicates that, generally, a contraction ratio of C = 0.9 yielded the least favorable thrust-to-power ratio, followed by a contraction ratio of C = 0.93, which can be attributed to relatively high air blockage causing increased pressure drag. Moreover, configurations with the inner shroud positioned closer to the rotor, where the inner shroud's effect is more dominant and effective, resulted in higher thrust-to-power ratios. Only five configurations yielded thrust-to-power ratios higher than that of the single exit shroud, with the L2D90C96Z1 configuration attaining the largest value.

Fig. 7 indicates that an inlet diameter of $0.95D_R$ for the inner shroud has a negative impact on the thrust- to-power ratio, while $0.9D_R$ shows a better influence, and $0.85D_R$ is not as favorable. To elucidate the reasons behind the differences in total thrust-to-power ratio, the downwash velocity contour at the exit plane of the main shroud is plotted to illustrate distinctions between the single exit shroud and dual exit shroud configurations. Considering the general effect of the two selected lengths (L_1&L_2), it depends on the inlet diameter of the inner shroud. The main difference between the longer length and the shorter one is that the shorter length is more effective. However, for an inlet diameter of $0.95D_R$, the longer length (L_1) exhibits a superior thrust-to-power ratio compared to the shorter length value (L_2). The downwash velocity contour at the midplane of the stationary zone is plotted for L1D95C96Z1 and L2D95C96Z1 and compared to SES in Fig. 8.

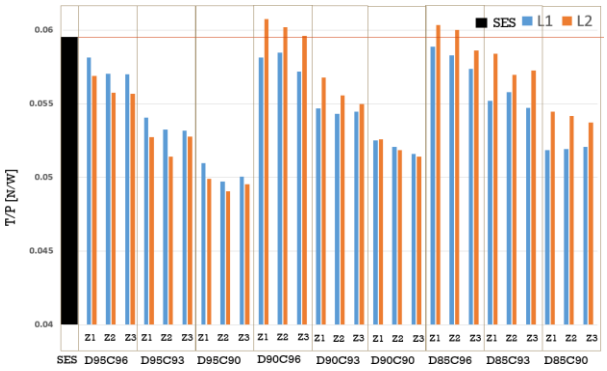

Fig. 7. Total thrust to total power ratio.

It is apparent from Fig. 8 that early separation occurs at the main shroud's inner walls of the single exit shroud with deviated airflow within the 95% of the rotor diameter. This can also be realized from Fig. 9 which shows the downwash velocity contour at the main shroud's exit plane for SES & DES (L2D95C96Z1). By comparing the velocity contours for DES (L1D95C96Z1) and DES (L2D95C96Z1) with that of the single exit shrouds in Fig. 8, it becomes apparent that the shorter length inner shroud is considered not only a source of drag but also results in flow disturbances and higher wake resulting in a lower thrust-to-power ratio. Furthermore, when compared to the larger length, the shorter inner shroud does not efficiently divert the inflow to the main shroud's inner walls.

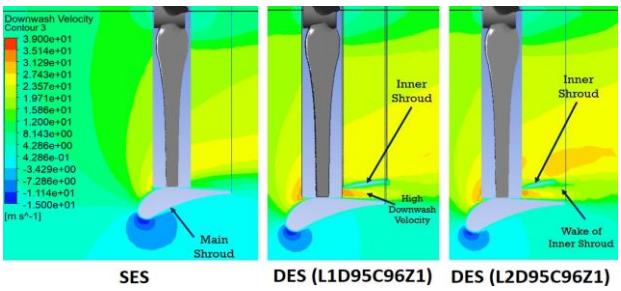

Fig. 8. Downwash velocity contour at the stationary zone's midplane.

Fig. 9 illustrates that there is essentially little effect on diverting the airflow into the low induced velocity sections, indicating the importance of having a greater mass flow rate in the outer channel. This explains why the separation and non-uniform power losses persist in the 95% DR case. Compared to Figs. 10 and 11, it can be realized that different values of the inlet diameter of the inner shroud affect the induced velocity distribution which in turn affect the nonuniform power losses. From the simulated results, it can be concluded that the inner shroud provides two significant advantages. Firstly, it prevents airflow separation from the main shroud's inner walls, and secondly, it yields a more uniform inflow, as intended, thereby reducing non-uniform inflow power losses. These advantages are particularly evident in the case of the L2D90C96Z1 configuration (Fig. 10). Among

the simulated 54 dual exit shroud configurations, it is observed that the L2D90C96Z1 configuration attains the largest thrust-to-power ratio; for some of the other configurations, the inner shroud proves to be disadvantageous. Fig. 10 demonstrates that the L2D90C96Z1 configuration resulted in the closest resemblance to a uniform inflow, coupled with the highest induced velocity compared to other dual exit shroud configurations. Fig. 11 also shows an improvement in downwash velocity uniformity when utilizing DES (L2D85C96Z1) over SES, although not as uniform as DES (L2D90C96Z1).

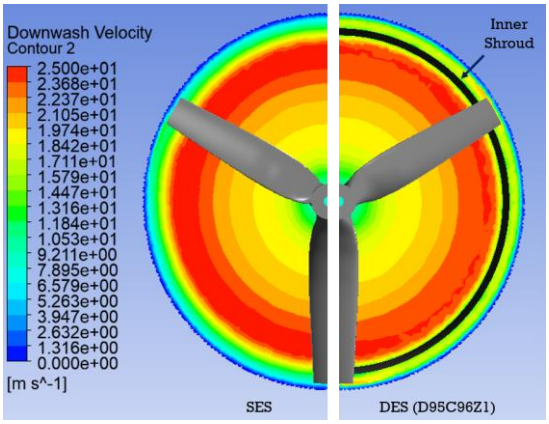

Fig. 9. Downwash velocity contour at the main shroud's exit plane for SES & DES (L2D95C96Z1).

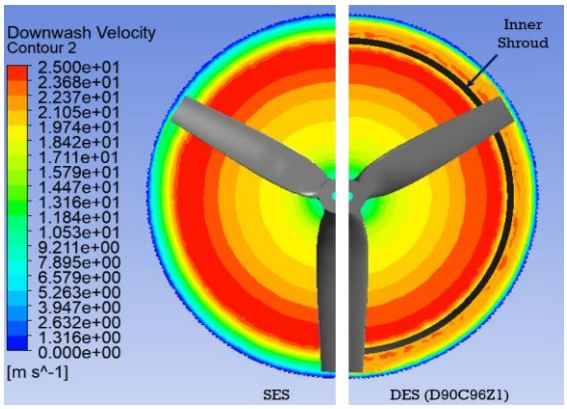

Fig. 10. Downwash velocity contour at the main shroud's exit plane for SES & DES (L2D90C96Z1).

The thrust-to-power ratio for the L2D90C96Z1 configuration exhibits an improvement of 2.13% over the single exit shroud. In comparison to a single-exit shrouded rotor, the dual-exit shrouded rotor of the L2D90C96Z1 configuration demonstrates an elevated induced velocity and shows more uniformity. More uniform flow results in decreased nonuniform power losses, which are directly substituted to the induced power, boosting the induced velocity in turn [29, 25]. Moreover, larger induced velocity leads to increased induced power and reduced profile power, consequently reducing the overall power as profile power is considered as power losses. Enhanced flow control is a significant advantage of directing additional airflow to the outer channel. This not only reduces separation but also increases the velocity of the air sucked around the shroud's input lips. The resistance of separation leads to a larger exit area, which increases the overall mass flow rate through the shrouded rotor configuration. Simultaneously, the increased air velocity around the shroud's inlet lips causes a higher suction pressure, which increases the shroud's thrust. This dual impact highlights the numerous benefits of using the novel inner channel.

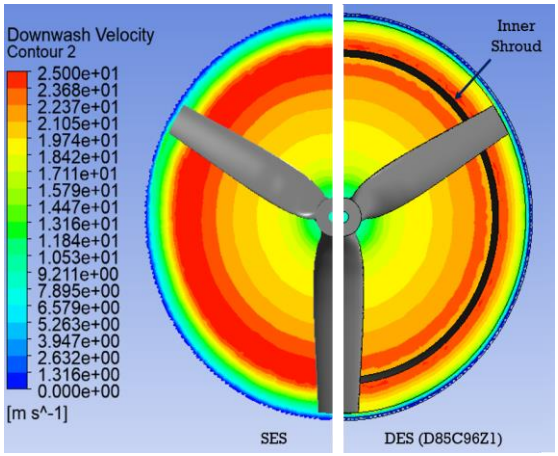

Fig. 11. Downwash velocity contour at the main shroud's exit plane for SES & DES (L2D85C96Z1).

VI. Conclusions

In this study, a novel inner shroud with a convergent shape was introduced into a shrouded rotor configuration to enhance overall performance by increasing the thrust-to-weight ratio. A comprehensive parametric study was conducted, exploring four key geometric parameters of the inner shroud: its length, inlet diameter, outlet diameter, and position relative to the shroud's diffuser. The investigation involved testing two lengths, three inlet diameters, three outlet diameters, and three positions. The inlet diameter was chosen as a percentage of the rotor diameter, the outlet diameter was determined relative to the inlet diameter, and both the length and position were defined relative to the main shroud's diffuser length. All simulations were executed at a consistent rotor rotational speed of 10,000 rpm.

The total thrust-to-power ratio for all configurations was compared with that of the single exit shroud. The systematic exploration of geometric parameters provides a nuanced understanding of their impact on performance metrics, offering valuable guidelines for designing shrouded rotor systems with enhanced efficiency. Interestingly, the shorter length exhibited superior performance compared to the longer length for the same contraction ratio, indicating its effectiveness in minimizing drag. An inlet diameter of $0.95D_R$ negatively impacted the thrust-to-power ratio, whereas $0.9D_R$ demonstrated the most favorable influence. Notably, a contraction ratio of $C = 0.96$ emerged as the most effective, yielding the best thrust-to-power ratio and simultaneously producing lower pressure drag. Moreover, configurations with the inner shroud positioned closer to

the rotor showcased higher thrust-to-power ratios, highlighting the enhanced effectiveness of the inner shroud in proximity to the rotor.

Increasing the induced velocity for rotors results in higher induced power and reduced profile power, ultimately leading to a decrease in total power. Notably, the dual exit shroud configuration with the best performance exhibited an improved thrust-to-power ratio by 2.13%. The success of this configuration can be attributed to two main advantages: firstly, a more uniform inflow downwash distribution, which mitigates power losses, and secondly, prevention of airflow separation from the main shroud's inner walls, contributing to increased thrust.

The proposed design investigated in this study not only improves aerodynamic performance but also addresses the long-standing difficulty of achieving an optimal balance between thrust and power consumption. This result not only fills important gaps in our understanding of shrouded rotor dynamics but also opens the door to transformative applications. The higher thrust-to-power ratio has enormous potential for expanding the capabilities of VTOL aircraft, particularly in applications that need increased efficiency, such as urban air mobility and surveillance. This unique method not only adds to the growth of rotorcraft technology but also provides the foundation for practical and significant advances in several real-world applications.

CONFLICT OF INTEREST

The authors declare no conflict of interest.

AUTHOR CONTRIBUTIONS

Abdallah Dayhoum has conducted the simulations and the analysis. Dr. Alejandro Ramirez-Serrano and Dr. Robert Martinuzzi have revised the work and developed the conclusions. All authors had conducted the research, analyzed the data and approved the final version.

REFERENCES

[1] M. Y. Zakaria, D. A. Pereira, S. A. Ragab, M. R. Hajj, and F. D. Marques, "An experimental study of added mass on a plunging airfoil oscillating with high frequencies at high angles of attack," in *Proc. 33rd AIAA Applied Aerodynamics Conference*, 2015, 3166.

[2] C. Park, A. Ramirez-Serrano, and M. Bisheban, "Estimation of time-varying inertia of aerial manipulators performing manipulation of unknown objects," in *Proc. the 10th International Conference of Control Systems, and Robotics (CDSR'23)*, Niagara Falls, Canada, June 01–03, 2023, 209. doi: 10.11159/cdsr23.209

[3] S. Mostafa and A. Ramirez-Serrano, "Three-dimensional flight corridor: An occupancy checking process for unmanned aerial vehicle motion planning inside confined spaces," *Robotics*, vol. 12, no. 5, 134, 2023.

[4] M. Taherinezhad and A. Ramirez-Serrano, "An enhanced incremental nonlinear dynamic inversion control strategy for advanced unmanned aircraft systems," *Aerospace*, vol. 10, no. 10, 843, 2023.

[5] A. Dayhoum, M. Y. Zakaria, and O. E. Abdelhamid, "Unsteady aerodynamic modeling and analysis of load distribution for helicopter rotor blades," *Journal of Aerospace Engineering*, vol. 35, no. 1, 04021106, 2022.

[6] A. Dayhoum, M. Y. Zakaria, and O. E. Abdelhamid, "Experimental investigation for a small helicopter in hovering and forward flight regimes," *Journal of Aerospace Engineering*, vol. 36, no. 4, 06023001, 2023.

[7] G. Hoffmann, H. Huang, S. Waslander, and C. Tomlin, "Quadrotor helicopter flight dynamics and control: Theory and experiment," in *Proc. AIAA Guidance, Navigation and Control Conference and Exhibit*, 2007, 6461.

[8] V. Hrishikeshavan, J. Black, and I. Chopra, "Design and performance of a quad-shrouded rotor micro air vehicle," *Journal of Aircraft*, vol. 51, no. 3, pp. 779–791, 2014.

[9] A. Akturk and C. Camci, "Tip clearance investigation of a ducted fan used in VTOL unmanned aerial vehicles—Part I: Baseline experiments and computational validation," *Journal of Turbomachinery*, vol. 136, no. 2, 2014.

[10] N. Amiri, A. Ramirez-Serrano, and B. Davies, "Nonlinear adaptive control of a new configuration of rotary wing unmanned aerial vehicle," in *Proc. 2012 25th IEEE Canadian Conference on Electrical and Computer Engineering (CCECE)*, IEEE, 2012, pp. 1–4.

[11] A. Kamal and A. Ramirez-Serrano, "Conceptual design of a highly-maneuverable transitional VTOL UAV with new maneuver and control capabilities," in *Proc. AIAA Scitech 2020 Forum*, 2020, 1733.

[12] C. Yang, P. Zhang, S. Jacob, E. Trigell, and M. Åbom, "Investigation of extended-tube liners for control of low-frequency duct noise," *AIAA Journal*, vol. 59, no. 10, pp. 4179–4194, 2021.

[13] A. Dayhoum, M. Y. Zakaria, and O. E. Abdelhamid, "Elastic torsion effects on helicopter rotor loading in forward flight," in *Proc. AIAA Scitech 2020 Forum*, 2020, 0507.

[14] A. Sacks and J. Burnell, "Ducted propellers—A critical review of the state of the art," *Progress in Aeronautical Sciences*, vol. 3, pp. 85–135, 1962.

[15] S. D'Angelo, F. Berardi, and E. Minisci, "Aerodynamic performances of propellers with parametric considerations on the optimal design," *The Aeronautical Journal*, vol. 106, no. 1060, 2002, pp. 313–320.

[16] P. Martin and C. Tung. (2024). Performance and flowfield measurements on a 10-inch ducted rotor VTOL UAV. Tech. Rep., Army Research Development and Engineering Command Moffett Field CA Aviation. [Online]. Available: https://ntrs.nasa.gov/citations/20050009943

[17] C. Thipyopas, R. Barènes, and J.-M. Moschetta, "Aerodynamic analysis of a multi-mission short-shrouded coaxial UAV: Part I-hovering flight," in *Proc. 26th AIAA Applied Aerodynamics Conference*, 2008, 6243.

[18] J. L. Pereira, "Hover and wind-tunnel testing of shrouded rotors for improved micro air vehicle design," Ph.D. dissertation, University of Maryland, College Park, 2008.

[19] M. P. Misiorowski, F. S. Gandhi, and A. A. Oberai, "Computational study of diffuser length on ducted rotor performance in edgewise flight," *AIAA Journal*, vol. 57, no. 2, pp. 796–808, 2019.

[20] A. Akturk and C. Camci, "Double-ducted fan as an effective lip separation control concept for vertical-takeoff-and-landing vehicles," *Journal of Aircraft*, vol. 59, no. 1, pp. 233–252, 2022.

[21] P. F. Yaggy and K. W. Mort, "A wind-tunnel investigation of a 4-foot-diameter ducted fan mounted on the tip of a semispan wing," *National Aeronautics and Space Administration*, 1961.

[22] Y. Li, K. Yonezawa, and H. Liu, "Effect of ducted multi-propeller Configuration on aerodynamic performance in quadrotor drone," *Drones*, vol. 5, no. 3, 101, 2021.

[23] B. L. Omkar, A. S. A. Doss, and T. C. Michael, "Design and analysis of coaxial ducted propulsion systems of unmanned aerial vehicles," *IOP Conference Series: Materials Science and Engineering*, IOP Publishing, 2021, vol. 1012, 012024.

[24] H. Cai, Z. Zhang, and S. Deng, "Numerical prediction of unsteady aerodynamics of a ducted fan unmanned aerial vehicle in hovering," *Aerospace*, vol. 9, no. 6, 318, 2022.

[25] W. Johnson, "Helicopter theory," *Courier Corporation*, 2012.

[26] M. Yavari, K. Gupta, M. Mehrandezh, and A. Ramirez-Serrano, "Optimal real-time trajectory control of a pitch-hover UAV with a two link manipulator," in *Proc. 2018 International Conference on Unmanned Aircraft Systems (ICUAS)*, IEEE, 2018, pp. 930–938.

[27] M. Majnoon, K. Samsami, M. Mehrandezh, and A. Ramirez-Serrano, "Mobile-target tracking via highly-maneuverable VTOL

UAVs with EO vision," in *Proc. 2016 13th Conference on Computer and Robot Vision (CRV)*, IEEE, 2016, pp. 260–265.
[28] M. Taherinezhad, A. Ramirez-Serrano, and A. Abedini, "Robust trajectory-tracking for a bi-copter drone using indi: A gain tuning multi-objective approach," *Robotics*, vol. 11, no. 5, 86, 2022.
[29] G. J. Leishman, *Principles of Helicopter Aerodynamics with CD Extra*, Cambridge University Press, 2006.